



Time-domain analysis of gravity dam–reservoir interaction using high-order doubly asymptotic open boundary

Xiang Wang^a, Feng Jin^a, Suriyon Prempramote^b, Chongmin Song^{b,*}

^a Department of Hydraulic Engineering, Tsinghua University, Beijing 100084, China

^b School of Civil and Environmental Engineering, University of New South Wales, Sydney, NSW 2052, Australia

ARTICLE INFO

Article history:

Received 23 October 2009

Accepted 17 January 2011

Available online 18 February 2011

Keywords:

Dam–reservoir interaction

Doubly asymptotic

Continued fraction

Open boundary

Transmitting boundary

ABSTRACT

A procedure for the time-domain analysis of gravity dam–reservoir interaction is proposed. The dam and a part of the reservoir with irregular geometry are modeled with finite elements. A high-order doubly asymptotic open boundary condition is developed to model the remaining part of the reservoir simplified as a semi-infinite layer of constant depth. This open boundary is temporally local, stable and converges rapidly as the order increases. It is directly coupled with the commercial software ABAQUS by using a sequential staggered implicit-implicit partition algorithm. Numerical examples demonstrate the high accuracy and long-time stability of the proposed technique.

© 2011 Elsevier Ltd. All rights reserved.

1. Introduction

The computation of hydrodynamic pressure on dams is necessary and important in the analysis of dam–reservoir interaction under earthquakes. Research in this area was pioneered by Westergaard [1]. He derived the analytical solution for a rigid dam with a vertical upstream surface under a horizontal harmonic ground motion. The added-mass method originated from his paper has influenced the engineering design of dams since then. In 1967, Chopra [2] developed an analytical formulation for the hydrodynamic pressure of compressible water on a rigid dam with a vertical upstream face under both horizontal and vertical earthquake excitation. When the upstream face of a dam is inclined, water is often simplified as being incompressible so that an analytical solution can be derived. For example, Chwang [3] presented an exact solution for a rigid dam with an inclined upstream face of constant slope by using a two-dimensional potential theory. In the companion paper, Chwang and Housner [4] employed the momentum-balance principle to solve the same problem approximately. As the dam is assumed to be rigid in the above studies, the effect of dam–reservoir interaction cannot be considered. Chopra and his coworkers [5,6] were the first to study the effects of flexible gravity dam–reservoir interaction by employing the first few modes of vibration of the dam obtained with an empty reservoir.

Analytical solutions are only available for reservoirs of regular geometries, such as semi-infinite layers or prisms. When the reser-

voir geometry is irregular, numerical methods such as the finite element method are necessary to analyze the dam–reservoir interaction. Substructure method is often applied (see Fig. 1). The part of the reservoir with irregular geometry, called the near field, is discretized with finite elements. To reduce the computational cost, the finite element mesh is truncated at a distance from the dam. The remaining part of the reservoir, called the far field, is simplified as a semi-infinite layer with constant depth. The near and far fields are coupled at the truncated boundary by satisfying the equations of motion and continuity. Various methods have been developed to model the far field. Saini, Bettess and Zienkiewicz [7] proposed the infinite element to analyze the two-dimensional response of reservoir–dam system subjected to horizontal ground motions. Chopra and his coworkers [8,9] developed efficient procedures to analyze dam–reservoir interaction in the frequency domain. The finite element discretization on the truncated boundary was combined with a continuum representation in the infinite direction of the reservoir.

A direct time-domain analysis is required when the dam exhibits nonlinear material behavior, for example, under earthquakes. Zienkiewicz and Bettess [10] studied fluid–structure interaction in the time domain by using Sommerfeld radiation condition to approximate the far field. Tsai, Lee and Ketter [11] proposed an accurate implicit semi-analytical transmitting boundary in the time domain. Tsai and Lee [12] established the corresponding time-domain models for the interaction analysis of dam–reservoir system by using the substructure method. This approach is temporally global, i.e. requires the evaluation of convolution integrals. It is expensive in computer time and memory for long-time analyses.

* Corresponding author. Tel.: +61 2 9385 5021; fax: +61 2 9385 6139.

E-mail address: c.song@unsw.edu.au (C. Song).

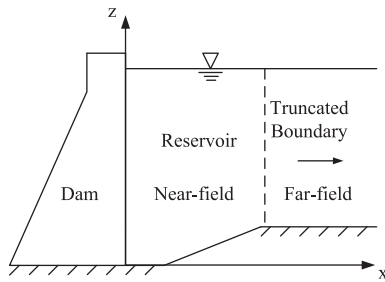


Fig. 1. A typical gravity dam–reservoir system.

To improve computational efficiency, Yang, Tsai and Lee [13] developed the explicit time-domain transmitting boundary which employed only a few eigenmodes in the evaluation of the convolution integrals. When the boundary element method [14–16] is applied to a direct time-domain analysis, the formulation is spatially and temporally global, which hinders its application to long-time computations of large-scale engineering problems.

Since mid-1990s, high-order transmitting boundaries have been proposed for the scalar wave equation. There is an extensive literature on this subject (see [17,18]). The high-order transmitting boundaries are constructed to absorb propagating waves radiating energy. The formulations are temporally local and more efficient than global procedures. They are reported not to suffer from instability plagued earlier versions of high-order transmitting boundaries. For problems of two- and three-dimensional cavities, they are shown to converge as the order increases. It is demonstrated by Prempramote et al. [19] that these transmitting boundaries are singly asymptotic at the high-frequency limit. They are efficient for radiative fields where all of the field energy is propagating out to infinity [20]. However, a semi-infinite reservoir with constant depth has a cut-off frequency. When the excitation frequency is close to or below the cut-off frequency, the wave field is not radiative. The high-order transmitting boundaries break down at low frequencies in a frequency domain analysis or at late times in a time domain analysis [19].

One advance towards the modeling of an unbounded domain with possible presence of non-radiative wave fields is the introduction of doubly asymptotic boundaries [20–24]. The dynamic stiffness of the doubly asymptotic boundaries is selected to fit the dynamic stiffness of the unbounded domain at both the high-frequency limit and the low-frequency limit (i.e. statics). The resulting formulation is spatially global. The highest order reported in the literature is three [25]. Another technique is the time-domain realisation of the dynamic stiffness obtained in the frequency domain developed by Ruge, et al. [26] and Alpert, et al. [27]. A rational approximation of the dynamic stiffness is constructed by curve-fitting. When it is transformed to the time domain, a recursive formula is obtained. Birk and Ruge [28] applied such a technique to the dam–reservoir interaction analysis. Accurate results can be obtained for long-time computations, but curve fitting by means of a least-squares process has to be performed for each order of the rational approximation.

Another popular technique for modeling wave propagation is the perfectly matched layer [29,30]. The performance of the perfectly matched layer is compared with that of a high-order transmitting boundary in Reference [27].

Very recently, Prempramote et al. [19] proposed a high-order doubly asymptotic open boundary condition for the one-dimensional scalar wave equation by extending the work in Ref. [31]. The open boundary condition is constructed directly from the differential equation of the dynamic stiffness matrix of an unbounded domain without evaluating its solution at discrete frequencies.

This high-order doubly asymptotic boundary is capable of accurately mimicking the unbounded domain over the entire frequency range (i.e. from zero to infinity). For a one-dimensional problem corresponding to one mode of the horizontal layer, the coefficients of the open boundary condition are explicitly given. A boundary condition of any order can be constructed straightforwardly. Excellent accuracy and stability are observed for long-time transient analysis.

The purpose of this paper is to extend the doubly asymptotic open boundary condition by Prempramote et al. in Ref. [19] to the analysis of the hydrodynamic pressure of a semi-infinite reservoir with constant depth. To facilitate the coupling with a commercial finite element package, the formulation of the open boundary condition is split into two parts. The first part is shown to be the simple Sommerfeld radiation boundary, also called the viscous boundary in the dynamic soil–structure interaction analysis, which is spatially and temporally local. It can be included in the damping matrix of the system. The second part includes all the high-order terms and is governed by a system of first-order ordinary differential equations. This part can be interpreted as external forces applied on the truncated boundary. Applying a sequential staggered implicit-implicit partition algorithm, the external forces are determined by the responses of the truncated boundary at the previous time station. This formulation does not modify the element connectivity and allows the direct coupling with a commercial finite element software package supporting two-way data exchange. This open boundary condition is implemented in the general-purpose finite element software ABAQUS to analyze gravity dam–reservoir interaction.

This paper is organized as follows. In Section 2, the finite element formulation of dam–reservoir system is addressed. In Section 3, the scaled boundary finite element method is applied to derive a semi-discrete governing equation on the truncated boundary. In Section 4, a modal transformation is performed leading to a set of uncoupled equations for modal dynamic stiffness. In Section 5, the doubly asymptotic continued fraction solution of the dynamic stiffness is presented. In Section 6, a high-order doubly asymptotic open boundary condition is constructed by introducing auxiliary variables. In Section 7, the numerical implementation of the open boundary condition and the coupling with ABAQUS are addressed. In Section 8, numerical examples of a rigid dam and a flexible dam are presented. In the final section, conclusions are stated.

2. Finite element model of dam–reservoir system

A two-dimensional reservoir is addressed (Fig. 1). The water in the reservoir is assumed to be compressible, inviscid and irrotational with a small amplitude movement. The hydrostatic body force is not considered in this paper as it can be simply superimposed to the hydrodynamic pressure. The acceleration vector of water particles is denoted as $\{\ddot{u}\} = [\ddot{u}_x(x, z, t), \ddot{u}_z(x, z, t)]^T$ and the hydrodynamic pressure as $p = p(x, z, t)$. The reservoir is divided into a near field including the irregular geometry and a far field extending to infinity with constant depth. The dam with possibly nonlinear material property and the near-field reservoir are modeled by finite elements. The hydrodynamic pressure p in the reservoir where the water is treated as acoustic fluid satisfies the scalar wave equation

$$\Delta p = \frac{1}{c^2} \frac{\partial^2 p}{\partial t^2} \quad (1)$$

with the Laplace operator Δ and the compression wave velocity

$$c = \sqrt{\frac{K}{\rho}}, \quad (2)$$

where K is the bulk modulus of water and ρ is the mass density. On the dam–reservoir interface, the pressure should satisfy the boundary condition (n stands for the outward normal of the boundary)

$$\frac{\partial p}{\partial n} = -\rho \ddot{u}_n. \tag{3}$$

The effect of surface waves on the hydrodynamic pressure on a dam is considered to be negligible. The boundary condition on the free surface is written as

$$p = 0. \tag{4}$$

At the reservoir bottom,

$$\frac{\partial p}{\partial n} = 0 \quad \text{or} \quad \ddot{u}_n = 0 \tag{5}$$

applies. At infinity, the radiation condition

$$\frac{\partial p}{\partial n} = -\frac{\dot{p}}{c}, \tag{6}$$

should be satisfied.

Without considering the material damping, the finite element formulation for the dam–reservoir system can be partitioned as

$$\begin{bmatrix} [M_s] & 0 & 0 \\ -[Q_{fs}] & [M_{ff}] & [M_{fb}] \\ 0 & [M_{bf}] & [M_{bb}] \end{bmatrix} \begin{Bmatrix} \{\dot{u}_s\} \\ \{\dot{p}_f\} \\ \{\dot{p}_b\} \end{Bmatrix} + \begin{bmatrix} [K_s] & [Q_{sf}] & 0 \\ 0 & [K_{ff}] & [K_{fb}] \\ 0 & [K_{bf}] & [K_{bb}] \end{bmatrix} \begin{Bmatrix} \{u_s\} \\ \{p_f\} \\ \{p_b\} \end{Bmatrix} = \begin{Bmatrix} \{f_s\} \\ \{f_f\} \\ -\{r\} \end{Bmatrix}, \tag{7}$$

where $[M]$ stands for the mass matrix, $[K]$ for the static stiffness matrix, $[Q]$ for the coupling matrix between solid and acoustic fluid and $\{f\}$ for the external force vector. Subscript s denotes degrees of freedom on the dam structure, subscript f denotes the degrees of freedom of the near-field water except for those on the truncated boundary that are denoted by the subscript b . Denoting the interaction load applied to the semi-infinite reservoir by the near-field water as $\{r\}$, the external load applied to the near-field water on the truncated boundary is equal to $-\{r\}$. The mass and stiffness matrices of water treated as acoustic fluid are expressed in ABAQUS as

$$[M_f] = \int_{V_f} \frac{1}{K} [N]^T [N] dV, \tag{8}$$

$$[K_f] = \int_{V_f} \frac{1}{\rho} \left(\frac{\partial [N]^T}{\partial x} \frac{\partial [N]}{\partial x} + \frac{\partial [N]^T}{\partial z} \frac{\partial [N]}{\partial z} \right) dV, \tag{9}$$

$$\{f_f\} = \int_{S_f} \frac{1}{\rho} [N] \frac{\partial p}{\partial x} dS, \tag{10}$$

where $[N]$ are the shape functions of finite elements. In order to solve Eq. (7) for the dam–reservoir system, the relationship between the interaction load $\{r\}$ and the hydrodynamic pressure $\{p\}$ of the semi-infinite reservoir is required, and is presented in the following sections.

3. Scaled boundary finite element method for semi-infinite reservoir with constant depth

The scalar wave equation in a semi-infinite reservoir with constant depth (far field) can be solved analytically in the frequency domain by the method of separation of variables. To facilitate the coupling with the finite elements of the near-field reservoir, a semi-analytical method is employed in this paper. The reservoir is discretized along its depth by elements that have the same nodes and shape functions as the finite elements. Several derivations leading to similar semi-analytical approaches exist (see, e.g.,

Lysmer and Wass [32]; Song and Wolf [33]; Birk and Ruge [28]). The scaled boundary finite-element method, developed to model unbounded domains with arbitrary shape [33], is selected in this paper considering the possibility of further extension of the present technique to problems with more complex geometry. The derivation of scaled boundary finite element method for elastodynamics is detailed in [33,34]. In this paper, the derivation is summarized for the two-dimensional semi-infinite reservoir with a vertical boundary (Fig. 2). Streamlined expressions are presented for this special case.

The scalar wave equation in Eq. (1) is expressed as the equation of motion

$$\{L\}p + \rho\{\ddot{u}\} = 0, \tag{11}$$

where $\{L\} = [\partial/\partial x \quad \partial/\partial z]^T$ is the differential operator and ρ the mass density, and the equation of continuity considering the volumetric stress–strain relationship of compressible water is written as

$$\{L\}^T\{\ddot{u}\} = -\frac{1}{K} \frac{\partial^2 p}{\partial t^2}. \tag{12}$$

The vertical boundary of the semi-infinite reservoir is specified by a constant coordinate x_b . It is discretized by one-dimensional elements (Fig. 2(a)). A typical element is shown in Fig. 2(b). The vertical coordinates of the nodes of an element are arranged in $\{z_b\}$. The geometry of an element is interpolated using the shape functions $[N(\eta)]$ formulated in the local coordinate η as

$$z_b(\eta) = [N(\eta)]\{z_b\}. \tag{13}$$

The Cartesian coordinates of a point (x, z) inside the semi-infinite reservoir are expressed as

$$x(\xi) = x_b + \xi, \quad z(\xi, \eta) = z_b(\eta) = [N(\eta)]\{z_b\}, \tag{14}$$

where the coordinate ξ is equal to 0 on the vertical boundary. The Jacobian matrix for the coordinate transformation from (x, z) to (ξ, η) is expressed as

$$[J(\eta)] = \begin{bmatrix} x_{,\xi} & z_{,\xi} \\ x_{,\eta} & z_{,\eta} \end{bmatrix} = \begin{bmatrix} 1 & 0 \\ 0 & z_{b,\eta} \end{bmatrix}. \tag{15}$$

For a two-dimensional problem with a unit length in the third dimension,

$$dV = |J(\eta)| d\xi d\eta, \tag{16}$$

where $|J(\eta)|$ is the determinant of the Jacobian matrix. The partial differential operator defined in Eq. (11) is expressed as

$$\{L\} = [J(\eta)]^{-1} \begin{bmatrix} \frac{\partial}{\partial \xi} & \frac{\partial}{\partial \eta} \end{bmatrix}^T = \{b^1\} \frac{\partial}{\partial \xi} + \{b^2(\eta)\} \frac{\partial}{\partial \eta} \tag{17}$$

with

$$\{b^1\} = \begin{Bmatrix} 1 \\ 0 \end{Bmatrix}, \quad \{b^2(\eta)\} = \frac{1}{|J(\eta)|} \begin{Bmatrix} 0 \\ 1 \end{Bmatrix}. \tag{18}$$

The governing differential equations in the local coordinates (ξ, η) are specified by Eq. (12) with the differential operator $\{L\}$ in Eq. (17).

Along horizontal lines passing through a node on the boundary, the nodal hydrodynamic pressure functions $\{p\} = \{p(\xi, t)\}$ are introduced. The nodal pressure on the boundary follows as $\{p_b(t)\} = \{p(\xi = 0, t)\}$. Isoparametric elements are used in the vertical direction. One element S^e on the boundary with the corresponding horizontal strip shown in Fig. 2(b) is addressed. The hydrodynamic pressure field $p = p(\xi, \eta, t)$ is obtained by interpolating the nodal pressure functions

$$p = [N(\eta)]\{p\}. \tag{19}$$

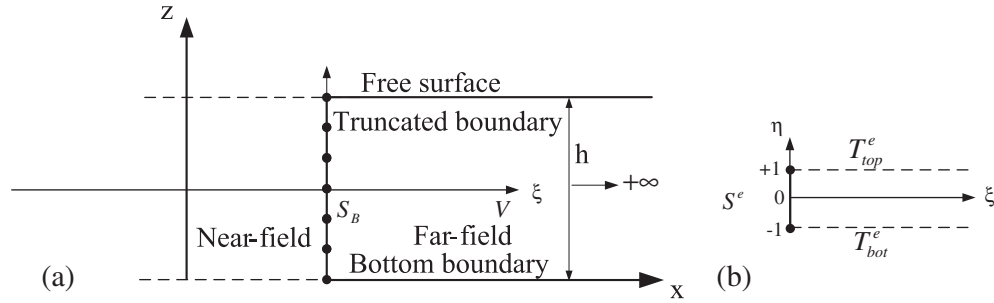


Fig. 2. Semi-discretization of semi-infinite reservoir with constant depth.

For an acoustic fluid, the relationship between acceleration and pressure is equivalent to that between stress and displacement in stress analysis. Substituting Eqs. (19) and (17) into Eq. (11), the acceleration $\{\ddot{u}\} = \{\ddot{u}(\xi, \eta)\}$ is expressed as

$$\{\ddot{u}\} = -\frac{1}{\rho} ([B^1(\eta)]\{p\}_{,\xi} + [B^2(\eta)]\{p\}) \quad (20)$$

with

$$[B^1(\eta)] = \{b^1\}[N(\eta)], \quad [B^2(\eta)] = \{b^2(\eta)\}[N(\eta)]_{,\eta}. \quad (21)$$

Galerkin's weighted residual method is applied. Eq. (12) is multiplied by a weighting function $w = w(\xi, \eta)$ and integrated over the semi-infinite strip corresponding to the element (Fig. 2(b))

$$\int_V w\{b^1\}^T \{\ddot{u}_{,\xi}\} dV + \int_V w\{b^2\}^T \{\ddot{u}_{,\eta}\} dV + \int_V w \frac{1}{K} \frac{\partial^2 p}{\partial t^2} dV = 0. \quad (22)$$

Using Eq. (16) and integrating the second term of Eq. (22) over η by parts yield

$$\int_0^\infty \left(\int_{-1}^1 \left(w\{b^1\}^T \{\ddot{u}_{,\xi}\} - w_{,\eta} \{b^2(\eta)\}^T \{\ddot{u}\} + w \frac{1}{K} \ddot{p} \right) \times |J(\eta)| d\eta + w\{b^2(\eta)\}^T \{\ddot{u}\} |J(\eta)|_{-1} \right) d\xi = 0. \quad (23)$$

Eq. (23) is satisfied by setting the integrand of the integral over ξ equal to zero

$$\int_{-1}^1 \left(w\{b^1\}^T \{\ddot{u}_{,\xi}\} - w_{,\eta} \{b^2(\eta)\}^T \{\ddot{u}\} + w \frac{1}{K} \ddot{p} \right) \times |J(\eta)| d\eta + w\{b^2(\eta)\}^T \{\ddot{u}\} |J(\eta)|_{-1} = 0. \quad (24)$$

This corresponds to enforcing the scalar wave equation exactly in the horizontal direction. Note that no volume integrals are present in Eq. (24).

The weighting function is constructed in the same way as the hydrodynamic pressure (Eq. (19))

$$w(\xi, \eta) = [N(\eta)]\{w(\xi)\}. \quad (25)$$

Substituting Eq. (25) into Eq. (24) yields, for arbitrary $\{w(\xi)\}$,

$$\int_{-1}^1 [B^1(\eta)]^T \{\ddot{u}_{,\xi}\} |J(\eta)| d\eta - \int_{-1}^1 [B^2(\eta)]^T \{\ddot{u}\} |J(\eta)| d\eta + \int_{-1}^1 [N(\eta)]^T \frac{1}{K} \ddot{p} |J(\eta)| d\eta + \{T\} = 0, \quad (26)$$

where $\{T\}$ is the equivalent nodal acceleration vector resulting from the acceleration distribution along the top and bottom of the strip

$$\{T\} = [N(\eta)]^T \{b^2(\eta)\}^T \{\ddot{u}\} |J(\eta)|_{-1}^{\pm 1}. \quad (27)$$

Substituting Eq. (20) into Eq. (26) leads to the scaled boundary finite element equation in hydrodynamic pressure

$$[E^0]\{p\}_{,\xi\xi} - [E^2]\{p\} - [M^0]\{\ddot{p}\} - \{T\} = 0, \quad (28)$$

where $[E^0]$, $[E^2]$ and $[M^0]$ are coefficient matrices

$$[E^0] = \int_{-1}^1 [B^1(\eta)]^T \frac{1}{\rho} [B^1(\eta)] |J(\eta)| d\eta = \int_{-1}^1 [N(\eta)]^T \frac{1}{\rho} [N(\eta)] |J(\eta)| d\eta, \quad (29a)$$

$$[E^2] = \int_{-1}^1 [B^2(\eta)]^T \frac{1}{\rho} [B^2(\eta)] |J(\eta)| d\eta = \int_{-1}^1 [N(\eta)]_{,\eta}^T \frac{1}{\rho} [N(\eta)]_{,\eta} \frac{1}{|J(\eta)|} d\eta, \quad (29b)$$

$$[M^0] = \int_{-1}^1 [N(\eta)]^T \frac{1}{K} [N(\eta)] |J(\eta)| d\eta = \frac{1}{c^2} [E^0]. \quad (29c)$$

The horizontal strips corresponding to the individual elements on boundary are assembled. The nodal acceleration vectors $\{T\}$ cancel at the common boundaries. On the bottom of the reservoir, the nodal acceleration vanishes (Eq. (5)). After enforcing the boundary condition $p(\xi, t) = 0$ on the free surface, the scaled boundary finite element equation for the two-dimensional semi-infinite reservoir with constant depth is expressed as

$$[E^0]\{p\}_{,\xi\xi} - [E^2]\{p\} - \frac{1}{c^2} [E^0]\{\ddot{p}\} = 0. \quad (30)$$

The standard numerical integration techniques in the finite element method are directly applicable to evaluate these coefficient matrices. Like the static stiffness and mass matrices in the finite element method, the coefficient matrices $[E^0]$ and $[E^2]$ are sparse and positive definite.

For acoustic fluid, the acoustic nodal load vector $\{r\} = \{r(\xi, t)\}$ on a vertical surface with a constant ξ is expressed as

$$\{r\} = -[E^0]\{p\}_{,\xi}. \quad (31)$$

It is the equivalent nodal vector of acceleration distribution based on virtual work principle. Assuming the time-harmonic response $\{p(\xi, t)\} = \{P(\xi, \omega)\}e^{+i\omega t}$ (ω is the excitation frequency) with the amplitudes of the hydrodynamic pressure $\{P\} = \{P(\xi, \omega)\}$, Eq. (30) is transformed into the frequency domain as

$$[E^0]\{P\}_{,\xi\xi} - [E^2]\{P\} + \frac{\omega^2}{c^2} [E^0]\{P\} = 0. \quad (32)$$

The amplitudes of the acoustic nodal load $\{R\} = \{R(\xi, \omega)\}$ ($\{r(\xi, t)\} = \{R(\xi, \omega)\}e^{+i\omega t}$) are expressed as (Eq. (31))

$$\{R\} = -[E^0]\{P\}_{,\xi}. \quad (33)$$

4. Modal decomposition of scaled boundary finite element equation

The system of ordinary differential equations in Eq. (32) can be decoupled by a modal transformation. The modes are obtained from the following generalized eigenvalue problem (\bullet stands for a diagonal matrix)

$$[E^2][\Phi] = [E^0][\Phi] \langle \lambda_j^2 \rangle / h^2, \tag{34}$$

where $\langle \lambda_j^2 \rangle$ is the diagonal matrix of positive eigenvalues, $[\Phi]$ are the eigenvectors representing the modes, and h is a characteristic length (e.g. the depth of the layer) to non-dimensionlize the eigenvalues. The eigenvectors $[\Phi]$ are normalized as

$$[\Phi]^T [E^0][\Phi] = [I]. \tag{35}$$

Pre-multiplying Eq. (34) with $[\Phi]^T$ results in

$$[\Phi]^T [E^2][\Phi] = \langle \lambda_j^2 \rangle / h^2. \tag{36}$$

It is noted from Eq. (35) that the inverse of the eigenvector matrix can be obtained by using the matrix multiplication

$$[\Phi]^{-1} = [\Phi]^T [E^0]. \tag{37}$$

The amplitudes of the hydrodynamic pressures are expressed as a linear combination of the eigenvectors

$$\{P\} = [\Phi] \{\tilde{P}\}, \tag{38}$$

where $\{\tilde{P}\} = \{\tilde{P}(\xi, \omega)\}$ are the amplitudes of the modal hydrodynamic pressures. Substituting Eq. (38) into Eq. (32) pre-multiplied with $[\Phi]^T$ and using Eqs. (35) and (36) lead to a system of decoupled equations

$$\tilde{P}_{j,\xi\xi} + \frac{1}{h^2} (a_0^2 - \lambda_j^2) \tilde{P}_j = 0 \tag{39}$$

with dimensionless frequency

$$a_0 = \frac{\omega h}{c}, \tag{40}$$

where the index j indicates the modal number. Substituting Eq. (38) into Eq. (33), the acoustic nodal force vector is expressed as

$$\{R\} = -[E^0][\Phi] \{\tilde{P}\}_{,\xi}. \tag{41}$$

The amplitude of the modal nodal force vector $\{\tilde{R}\} = \{\tilde{R}(\xi, \omega)\}$ is defined as

$$\{\tilde{R}\} = -h \{\tilde{P}\}_{,\xi} \quad \text{or} \quad \tilde{R}_j = -h \tilde{P}_{j,\xi}. \tag{42}$$

Pre-multiplying Eq. (41) with $[\Phi]^T$ and using Eqs. (35) and (42) yield

$$\{\tilde{R}\} = h [\Phi]^T \{R\}. \tag{43}$$

This equation transforms the amplitude of the acoustic nodal force vector to the amplitude of the modal force vector. It can be used together with Eq. (42) to specify the boundary condition for the modal equation (Eq. (39)) from the prescribed amplitude of acoustic nodal force vector $\{R\}$.

Eq. (39) can be solved analytically. The key equations given in Ref. [19] are summarized in the following.

The modal dynamic stiffness coefficient $\tilde{S}_j(a_0)$ is defined as

$$\tilde{R}_j = \tilde{S}_j(a_0) \tilde{P}_j \tag{44}$$

with its solution equal to

$$\tilde{S}_j(a_0) = \sqrt{\lambda_j^2 - a_0^2}. \tag{45}$$

Note that the modal dynamic stiffness is independent of the horizontal coordinate ξ . Performing the inverse Fourier transformation of \tilde{P}_j determined from Eqs. (44) and (45) leads to

$$\tilde{p}_j(\xi, t) = \frac{c}{h} \int_0^t J_0 \left(\lambda_j \frac{c(t-\tau)}{h} \right) \tilde{r}_j(\xi, \tau) d\tau, \tag{46}$$

where J_0 is the zero order first kind Bessel function. Substituting Eq. (46) into Eq. (38) and using Eq. (43) yield

$$\{p(\xi, t)\} = c [\Phi] \int_0^t \left\langle J_0 \left(\lambda_j \frac{c(t-\tau)}{h} \right) \right\rangle [\Phi]^T \{r(\xi, \tau)\} d\tau. \tag{47}$$

When the time history of the nodal forces $\{r(\xi, t)\}$ is prescribed at a vertical boundary specified with a constant ξ , the nodal hydrodynamic pressure $\{p(\xi, t)\}$ can be computed by using Eq. (47). However, this equation is temporally global, and the Bessel function decays very slowly at a rate of $1/\sqrt{t}$. The computational effort increases rapidly with the number of time steps.

5. Doubly asymptotic continued fraction solution for modal dynamic stiffness

A temporally local open boundary condition is constructed in Reference [19] for a single mode of wave propagation. It is based on a doubly asymptotic solution of the modal dynamic stiffness coefficient $\tilde{S}_j(a_0)$. By eliminating \tilde{R}_j and \tilde{P}_j from Eqs. (39), (42) and (44), an equation for the dynamic stiffness coefficient $\tilde{S}_j(a_0)$ is derived

$$(\tilde{S}_j(a_0))^2 + a_0^2 - \lambda_j^2 = 0. \tag{48}$$

The solution of Eq. (48) is expressed as a doubly asymptotic continued fraction. An order M_H high-frequency continued fraction is constructed first

$$\tilde{S}_j(a_0) = (ia_0) \tilde{C}_{\infty j} - \frac{\lambda_j^2}{(ia_0) \tilde{Y}_{1j}^{(1)} - \frac{\lambda_j^2}{(ia_0) \tilde{Y}_{1j}^{(2)} - \frac{\lambda_j^2}{\dots - \frac{\lambda_j^2}{(ia_0) \tilde{Y}_{1j}^{(M_H)} - \frac{\lambda_j^2}{\tilde{Y}_{j(M_H+1)}(a_0)}}}}, \tag{49}$$

which is equivalent to

$$\tilde{S}_j(a_0) = (ia_0) \tilde{C}_{\infty j} - \lambda_j^2 \left(\tilde{Y}_{1j}^{(1)}(a_0) \right)^{-1}, \tag{50a}$$

$$\tilde{Y}_j^{(i)}(a_0) = (ia_0) \tilde{Y}_{1j}^{(i)} - \lambda_j^2 \left(\tilde{Y}_j^{(i+1)}(a_0) \right)^{-1} \quad (i = 1, 2, \dots, M_H), \tag{50b}$$

where the constants $\tilde{C}_{\infty j}$ and $\tilde{Y}_{1j}^{(i)} (i = 1, 2, \dots, M_H)$ are determined by satisfying Eq. (48) at the high-frequency limit $a_0 \rightarrow +\infty$. Substituting Eq. (50a) into Eq. (48) results in an equation in terms of a power series of (ia_0)

$$(ia_0)^2 \left(\tilde{C}_{\infty j}^2 - 1 \right) + \lambda_j^2 \left(-1 - 2(ia_0) \tilde{C}_{\infty j} \left(\tilde{Y}_{1j}^{(1)}(a_0) \right)^{-1} + \lambda_j^2 \left(\tilde{Y}_{1j}^{(1)}(a_0) \right)^{-2} \right) = 0. \tag{51}$$

This equation is satisfied by setting, in descending order, the two terms to zero. The damping coefficient $\tilde{C}_{\infty j}$ is obtained from the first term. To satisfy the radiation condition, the positive solution is chosen

$$\tilde{C}_{\infty j} = 1. \tag{52}$$

The second term of Eq. (51) is an equation for the residual term $\tilde{Y}_j^{(1)}(a_0)$ as $\tilde{C}_{\infty j}$ is known. To derive a recursive formula for determining the constants of the continued fraction, it is rewritten as the $i = 1$ case of

$$\lambda_j^2 - 2b_{1j}^{(i)} (ia_0) \tilde{Y}_j^{(i)}(a_0) - \left(\tilde{Y}_j^{(i)}(a_0) \right)^2 = 0 \quad (i = 1, 2, \dots, M_H) \tag{53}$$

with the constant

$$b_{1j}^{(1)} = 1. \tag{54}$$

Substituting Eq. (50b) into Eq. (53) leads to an equation in terms of a power series of (ia_0)

$$-(ia_0)^2 \left((\tilde{Y}_{1j}^{(i)})^2 + 2b_{1j}^{(i)} \tilde{Y}_{1j}^{(i)} \right) + \lambda_j^2 \left(1 + 2(ia_0) (\tilde{Y}_{1j}^{(i)} + b_{1j}^{(i)}) (\tilde{Y}_j^{(i+1)}(a_0))^{-1} - \lambda_j^2 (\tilde{Y}_j^{(i+1)}(a_0))^{-2} \right) = 0. \tag{55}$$

Similar to the process from Eqs. (51)–(55), the coefficients in the continued fraction in Eq. (50b) are determined by solving Eq. (55) recursively

$$b_{1j}^{(i)} = (-1)^{i+1} \quad (i = 1, 2, \dots, M_H), \tag{56}$$

$$\tilde{Y}_{1j}^{(i)} = -2b_{1j}^{(i)} = (-1)^i 2 \quad (i = 1, 2, \dots, M_H). \tag{57}$$

Using Eqs. (52) and (57), the high-frequency continued fraction in Eq. (50a) is expressed as

$$\tilde{S}_j(a_0) = (ia_0) - \lambda_j^2 (\tilde{Y}_j^{(1)}(a_0))^{-1}, \tag{58a}$$

$$\tilde{Y}_j^{(i)}(a_0) = (-1)^i 2(ia_0) - \lambda_j^2 (\tilde{Y}_j^{(i+1)}(a_0))^{-1} \quad (i = 1, 2, \dots, M_H). \tag{58b}$$

It is shown in Prempramote et al. [19] that the high-frequency continued fraction does not converge below the cut-off frequency. To determine a solution that is valid over the whole frequency range, a low-frequency continued fraction solution is sought for the residual term $\tilde{Y}_j^{(M_H+1)}(a_0)$. Denoting the residual term for mode j as

$$\tilde{Y}_{Lj}(a_0) = \tilde{Y}_j^{(M_H+1)}(a_0). \tag{59}$$

The $i = M_H + 1$ case of Eq. (53) is rewritten as

$$\lambda_j^2 - 2b_{Lj}(ia_0)\tilde{Y}_{Lj}(a_0) - (\tilde{Y}_{Lj}(a_0))^2 = 0 \tag{60}$$

with the constant

$$b_{Lj} = b_{1j}^{(M_H+1)} = (-1)^{M_H}. \tag{61}$$

The continued fraction solution for $\tilde{Y}_{Lj}(a_0)$ at the low-frequency limit is written as

$$\tilde{Y}_{Lj}(a_0) = \tilde{Y}_{L0j}^{(0)} + (ia_0)\tilde{Y}_{L1j}^{(0)} - \frac{(ia_0)^2}{\tilde{Y}_{L0j}^{(1)} - \frac{(ia_0)^2}{\tilde{Y}_{L0j}^{(2)} - \frac{(ia_0)^2}{\tilde{Y}_{L0j}^{(3)} - \dots - \frac{(ia_0)^2}{\tilde{Y}_{L0j}^{(M_L)}}}}. \tag{62}$$

It is equivalent to

$$\tilde{Y}_{Lj}(a_0) = \tilde{Y}_{L0j}^{(0)} + (ia_0)\tilde{Y}_{L1j}^{(0)} - (ia_0)^2 (\tilde{Y}_{Lj}^{(1)}(a_0))^{-1}, \tag{63a}$$

$$\tilde{Y}_{Lj}^{(i)}(a_0) = \tilde{Y}_{L0j}^{(i)} - (ia_0)^2 (\tilde{Y}_{Lj}^{(i+1)}(a_0))^{-1} \quad (i = 1, 2, \dots, M_L). \tag{63b}$$

The coefficients $\tilde{Y}_{L1j}^{(0)}$ and $\tilde{Y}_{L0j}^{(i)}$ ($i = 0, 1, 2, \dots, M_L$) in Eq. (63) are determined by satisfying Eq. (60) at the low-frequency limit $a_0 \rightarrow 0$. Substituting Eq. (63a) into Eq. (60) leads to an equation in terms of a power series of (ia_0)

$$\left(\lambda_j^2 - (\tilde{Y}_{L0j}^{(0)})^2 \right) - (ia_0) \left(2b_{Lj}\tilde{Y}_{L0j}^{(0)} + 2\tilde{Y}_{L0j}^{(0)}\tilde{Y}_{L1j}^{(0)} \right) + (ia_0)^2 \left(-2b_{Lj}\tilde{Y}_{L1j}^{(0)} - (\tilde{Y}_{L1j}^{(0)})^2 + 2(\tilde{Y}_{L0j}^{(0)} + (ia_0)(\tilde{Y}_{L1j}^{(0)} + b_{Lj})) \right) \times \left(\tilde{Y}_{Lj}^{(1)}(a_0) \right)^{-1} - (ia_0)^2 (\tilde{Y}_{Lj}^{(1)}(a_0))^{-2} = 0. \tag{64}$$

As the low-frequency solution is being sought, Eq. (64) is satisfied by setting the coefficients of the power series to zero in ascending order. The constant term leads to two solutions for

$\tilde{Y}_{L0j}^{(0)}$, the one leading to the correct modal static dynamic stiffness $\tilde{S}_j(a_0 = 0) = \lambda_j$ should be chosen. Inspecting Eq. (49) with $\tilde{Y}_j^{(M_H+1)}(0) = \tilde{Y}_{L0j}(0) = \tilde{Y}_{L0j}^{(0)}$, the solution is

$$\tilde{Y}_{L0j}^{(0)} = (-1)^{M_H+1} \lambda_j. \tag{65}$$

For the coefficient of (ia_0) term in Eq. (64), using Eq. (61), the solution of $\tilde{Y}_{L1j}^{(0)}$ is

$$\tilde{Y}_{L1j}^{(0)} = (-1)^{M_H+1}. \tag{66}$$

The equation for the residual $\tilde{Y}_{Lj}^{(1)}(a_0)$ is expressed as the $i = 1$ case of

$$(ia_0)^2 - 2b_{Lj}^{(i)}\tilde{Y}_{Lj}^{(i)}(a_0) - (\tilde{Y}_{Lj}^{(i)}(a_0))^2 = 0 \quad (i = 1, 2, \dots, M_L) \tag{67}$$

with the constant

$$b_{Lj}^{(1)} = -b_{Lj}\lambda_j = (-1)^{M_H+1}\lambda_j. \tag{68}$$

After substituting Eq. (63b) into Eq. (67), following the procedure for constructing the continued fraction solution at high frequency, the solutions of $\tilde{Y}_{L0j}^{(i)}$ ($i = 1, 2, \dots, M_L$) are recursively obtained as

$$\tilde{Y}_{L0j}^{(i)} = (-1)^{M_H+i+1} 2\lambda_j \quad (i = 1, 2, \dots, M_L). \tag{69}$$

For an order M_L low-frequency solution, the residual $(ia_0)^2 (\tilde{Y}_{Lj}^{(M_L+1)}(a_0))^{-1}$ is neglected. Using Eqs. (65), (66) and (69), the low-frequency continued fraction solution in Eq. (63) is equal to

$$\tilde{Y}_{Lj}(a_0) = (-1)^{M_H+1}\lambda_j + (-1)^{M_H+1}(ia_0) - (ia_0)^2 (\tilde{Y}_{Lj}^{(1)}(a_0))^{-1}, \tag{70a}$$

$$\tilde{Y}_{Lj}^{(i)}(a_0) = (-1)^{M_H+i+1} 2\lambda_j - (ia_0)^2 (\tilde{Y}_{Lj}^{(i+1)}(a_0))^{-1} \quad (i = 1, 2, \dots, M_L). \tag{70b}$$

Combining the high-frequency solution (Eq. (49)) and the low-frequency solution (Eq. (62)) by using Eq. (59) yields the doubly asymptotic continued fraction solution. For example, the order $M_H = M_L = 2$ doubly asymptotic continued fraction solution for mode j is expressed as

$$\tilde{S}_j(a_0) = (ia_0) - \frac{\lambda_j^2}{-2(ia_0) - \frac{\lambda_j^2}{2(ia_0) - \frac{\lambda_j^2}{-\lambda_j - (ia_0) - \frac{(ia_0)^2}{2\lambda_j - \frac{(ia_0)^2}{-2\lambda_j}}}}}. \tag{71}$$

6. High-order doubly asymptotic open boundary

Following the procedure developed for the modal space in Reference [19], the acoustic force-pressure relationship in the time domain is formulated by using the continued fraction solution of the dynamic stiffness and introducing auxiliary variables. A system of first-order ordinary differential equations with symmetric coefficient matrices is obtained, which represents a temporally local open boundary condition.

Substituting the first term of the continued fraction solution (Eq. (58a)) into Eq. (44), the amplitude of modal force is written as

$$\tilde{R}_j = (ia_0)\tilde{P}_j - \lambda_j\tilde{P}_j^{(1)}, \tag{72}$$

where the auxiliary variable $\tilde{P}_j^{(1)}$ is defined in

$$\lambda_j\tilde{P}_j = \tilde{Y}_j^{(1)}(a_0)\tilde{P}_j^{(1)}. \tag{73}$$

Using Eqs. (43) and (72), the amplitude of nodal force vector is expressed as

$$h\{R\} = (ia_0)[\Phi]^{-T}\{\tilde{P}\} - [\Phi]^{-T}\langle\lambda_j\rangle\{\tilde{P}^{(1)}\}. \tag{74}$$

Substituting $\{\tilde{P}\} = [\Phi]^{-1}\{P\}$ (Eq. (38)) and $[E^0] = [\Phi]^{-T}[\Phi]^{-1}$ (Eq. (35)) into Eq. (74) leads to

$$h\{R\} = (ia_0)[E^0]\{P\} - [\Phi]^{-T}\langle\lambda_j\rangle\{\tilde{P}^{(1)}\}. \quad (75)$$

Substituting Eq. (58b) into Eq. (73) leads to

$$\lambda_j\tilde{P}_j = -2(ia_0)\tilde{P}_j^{(1)} - \lambda_j\tilde{P}_j^{(2)}, \quad (76)$$

where $\tilde{P}_j^{(2)}$ is defined as the $i = 1$ case in

$$\lambda_j\tilde{P}_j^{(i)} = \tilde{Y}_j^{(i+1)}(a_0)\tilde{P}_j^{(i+1)}. \quad (77)$$

Substituting $\{\tilde{P}\} = [\Phi]^{-1}\{P\}$ (Eq. (38)) into Eq. (76) formulated for all the modes yields

$$\langle\lambda_j\rangle[\Phi]^{-1}\{P\} = -2(ia_0)\{\tilde{P}^{(1)}\} - \langle\lambda_j\rangle\{\tilde{P}^{(2)}\}. \quad (78)$$

Substituting the remaining terms of the continued fraction solution in Eq. (58b) into Eq. (77) results in

$$\lambda_j\tilde{P}_j^{(i-1)} = (-1)^i 2(ia_0)\tilde{P}_j^{(i)} - \lambda_j\tilde{P}_j^{(i+1)} \quad (i = 2, 3, \dots, M_H) \quad (79)$$

The residual term of an order M_H high-frequency continued fraction solution given by Eq. (77) at $i = M_H$ is the initial term of the low-frequency continued fraction (Eq. (70a)). It is expressed as

$$\lambda_j\tilde{P}_j^{(M_H)} = \tilde{Y}_j^{(M_H+1)}(a_0)\tilde{P}_j^{(M_H+1)} = \tilde{Y}_{L_j}(a_0)\tilde{P}_{L_j}^{(0)} \quad (80)$$

with the auxiliary variable $\tilde{P}_{L_j}^{(0)} = \tilde{P}_j^{(M_H+1)}$. Substituting Eq. (70a) into Eq. (80) leads to

$$\lambda_j\tilde{P}_j^{(M_H)} = (-1)^{M_H+1}\lambda_j\tilde{P}_{L_j}^{(0)} + (-1)^{M_H+1}(ia_0)\tilde{P}_{L_j}^{(0)} - (ia_0)\tilde{P}_{L_j}^{(1)}, \quad (81)$$

where the auxiliary variable $\tilde{P}_{L_j}^{(1)}$ is defined in the $i = 1$ case of

$$(ia_0)\tilde{P}_{L_j}^{(i-1)} = \tilde{Y}_{L_j}^{(i)}(a_0)\tilde{P}_{L_j}^{(i)}. \quad (82)$$

Substituting Eq. (70b) into Eq. (82) leads to

$$(ia_0)\tilde{P}_{L_j}^{(i-1)} = (-1)^{M_H+i+1}2\lambda_j\tilde{P}_{L_j}^{(i)} - (ia_0)\tilde{P}_{L_j}^{(i+1)} \quad (i = 1, 2, \dots, M_L). \quad (83)$$

For an order M_L low-frequency continued fraction solution, $\tilde{P}_{L_j}^{(M_L+1)} = 0$ applies. Eqs. (75), (78), (79), (81) and (83) constitute a system of linear equations for the amplitude of nodal force vector $\{R\}$, the amplitude of nodal pressure vector $\{P\}$, and auxiliary variables $\{\tilde{P}^{(i)}\}$ ($i = 1, 2, 3, \dots, M_H$) and $\{\tilde{P}_{L_j}^{(i)}\}$ ($i = 0, 1, 2, 3, \dots, M_L$). This system of equations describes an acoustic nodal force–pressure relationship equivalent to the doubly asymptotic continued fraction solution of the modal dynamic stiffness. This formulation is linear in (ia_0) and can be directly transformed to the time domain. The inverse Fourier transforms of Eqs. (75), (78), (79), (81) and (83) divided by h are written as

$$\{r\} = \frac{1}{c}[E^0]\{\dot{p}\} - \frac{1}{h}[\Phi]^{-T}\langle\lambda_j\rangle\{\tilde{p}^{(1)}\}, \quad (84)$$

$$\frac{1}{h}\langle\lambda_j\rangle[\Phi]^{-1}\{p\} = -\frac{2}{c}\{\dot{p}^{(1)}\} - \frac{1}{h}\langle\lambda_j\rangle\{\tilde{p}^{(2)}\}, \quad (85)$$

$$\frac{1}{h}\lambda_j\tilde{p}_j^{(i-1)} = (-1)^i \frac{2}{c}\dot{p}_j^{(i)} - \frac{1}{h}\lambda_j\tilde{p}_j^{(i+1)} \quad (i = 2, 3, \dots, M_H), \quad (86)$$

$$\frac{1}{h}\lambda_j\tilde{p}_j^{(M_H)} = (-1)^{M_H+1}\frac{1}{h}\lambda_j\tilde{p}_{L_j}^{(0)} + (-1)^{M_H+1}\frac{1}{c}\dot{p}_{L_j}^{(0)} - \frac{1}{c}\dot{p}_{L_j}^{(1)}, \quad (87)$$

$$\frac{1}{c}\dot{p}_{L_j}^{(i-1)} = (-1)^{M_H+i+1}\frac{2}{h}\lambda_j\tilde{p}_{L_j}^{(i)} - \frac{1}{c}\dot{p}_{L_j}^{(i+1)} \quad (i = 1, 2, \dots, M_L). \quad (88)$$

Assembling Eqs. (84)–(88) leads to a system of first order ordinary differential equations with banded and symmetric coefficient matrices. This system of ordinary differential equations relating the interaction load $\{r\}$ and hydrodynamic pressure $\{p\}$ in the time domain is a temporally local high-order open boundary condition for the semi-infinite reservoir with constant depth. It is directly

established on the nodes of a vertical boundary. This boundary condition can be coupled seamlessly with finite elements. However, it introduces auxiliary variables as additional degrees of freedom. The coupling with commercial software packages is not feasible for a user without access to the source codes. To overcome this difficulty, the following sequential staggered implicit-implicit partition algorithm is adopted.

7. Numerical implementation in time domain

Substituting Eq. (84) into Eq. (7), the equation of motion of the dam–reservoir system considering the interaction between the near-field water and the semi-infinite reservoir is expressed as

$$\begin{bmatrix} [M_s] & 0 & 0 \\ -[Q_{fs}] & [M_{ff}] & [M_{fb}] \\ 0 & [M_{bf}] & [M_{bb}] \end{bmatrix} \begin{Bmatrix} \{\ddot{u}_s\} \\ \{\ddot{p}_f\} \\ \{\ddot{p}_b\} \end{Bmatrix} + \frac{1}{c} \begin{bmatrix} 0 & 0 & 0 \\ 0 & 0 & 0 \\ 0 & 0 & [E_0] \end{bmatrix} \begin{Bmatrix} \{\dot{u}_s\} \\ \{\dot{p}_f\} \\ \{\dot{p}_b\} \end{Bmatrix} + \begin{bmatrix} [K_s] & [Q_{sf}] & 0 \\ 0 & [K_{ff}] & [K_{fb}] \\ 0 & [K_{bf}] & [K_{bb}] \end{bmatrix} \begin{Bmatrix} \{u_s\} \\ \{p_f\} \\ \{p_b\} \end{Bmatrix} = \begin{Bmatrix} \{f_s\} \\ \{f_f\} \\ [\Phi]^{-T}\langle\lambda_j\rangle\{\tilde{p}^{(1)}\}/h \end{Bmatrix}. \quad (89)$$

Note that an additional damping term appears in Eq. (89). Comparing the expression of $[E^0]$ in Eq. (29a) with the Sommerfeld radiation condition (see also Eq. (6))

$$\frac{\partial p}{\partial x} = -\frac{\dot{p}}{c} \quad \text{i.e.} \quad \ddot{u}_x = -\frac{1}{\rho} \frac{\partial p}{\partial x} = \frac{\dot{p}}{\rho c} \quad (90)$$

it is found that the damping term is equivalent to the Sommerfeld radiation boundary, which is provided in ABAQUS. This term is therefore evaluated and assembled by the internal code of ABAQUS. The coupling term $[\Phi]^{-T}\langle\lambda_j\rangle\{\tilde{p}^{(1)}\}/h$ on the right-hand side of Eq. (89) represents the contribution of the high-order terms of the doubly asymptotic boundary. It can be regarded as an external load applied on the truncated boundary. When this term is set to zero, the high-order boundary condition degenerates to the Sommerfeld radiation boundary. As shown in Eq. (85), its value depends on the response history of the hydrodynamic pressure $\{p\}$. For efficiency consideration in the numerical implementation, the hydrodynamic pressure $\{p\}$ is transformed to the modal hydrodynamic pressure (Eq. (38))

$$\{\tilde{p}\} = [\Phi]^{-1}\{p\}. \quad (91)$$

Using Eq. (91) and multiplying Eq. (85) by h/λ_j leads to

$$\tilde{p}_j = -\frac{2h}{c\lambda_j}\dot{p}_j^{(1)} - \tilde{p}_j^{(2)}. \quad (92)$$

Eqs. (92), (86), (87) and (88) are decoupled for individual modes. For each mode, they are assembled as a system of ordinary differential equations for the auxiliary variables

$$[K_A]\{z_{A_j}(t)\} + \frac{h}{c\lambda_j}[C_A]\{\dot{z}_{A_j}(t)\} = \{f_{A_j}(t)\}, \quad (93)$$

where the vector $\{z_{A_j}(t)\}$ consists of the auxiliary variables of mode j (the semicolon “;” stands for the vertical concatenation of vectors)

$$\{z_{A_j}(t)\} = \{\tilde{p}_j^{(1)}; \dots; \tilde{p}_j^{(M_H)}; \tilde{p}_{L_j}^{(0)}; \tilde{p}_{L_j}^{(1)}; \dots; \tilde{p}_{L_j}^{(M_L)}\}. \quad (94)$$

The only nonzero entry on the right-hand side is the modal hydrodynamic pressure \tilde{p}_j determined from Eq. (91)

$$\{f_{A_j}(t)\} = \{-\tilde{p}_j; 0; \dots; 0; 0; 0; \dots; 0\}. \quad (95)$$

values, denoted as $\min(\text{Re}(\lambda_A))$, is plotted in Fig. 3 up to the order $M_H = M_L = 100$. It is observed that the real parts of all the eigenvalues λ_A are positive. As $\lambda_j c/h$ is always positive, Eq. (93) is asymptotically stable.

Eq. (89) for the near field and Eq. (93) for the far field are coupled by the auxiliary variables $\{\tilde{p}^{(1)}\}$. These two sets of equations are solved by a sequential staggered implicit-implicit partitioned procedure proposed in References [35,36]. Eq. (89) is integrated implicitly by using the trapezoidal rule to evaluate the hydrodynamic pressure. The value of the auxiliary variables $\{\tilde{p}^{(1)}\}$ at time station t_{n+1} is obtained from the last-solution extrapolation predictor [35,36]

$$\{\tilde{p}^{(1)}\}_{n+1}^p = \{\tilde{p}^{(1)}\}_n \tag{99}$$

The auxiliary variables $\{\tilde{p}^{(1)}\}$ are obtained by integrating Eq. (93) for prescribed hydrodynamic pressure $\{p\}$ (Eqs. (91) and (95)).

Based on the restart function of ABAQUS, a two-way data-exchange sequential coupling scheme is proposed to solve Eqs. (89) and (93) alternately. The algorithm proceeds as follows:

1. Initialize variables $\{u\}_0$ and $\{p\}_0$ in Eq. (89) and $\{z_{A,j}\}_0 = 0$ for each mode in Eq. (93);
2. Extract $\{\tilde{p}^{(1)}\}_n$ from $\{z_{A,j}\}_n$ of each mode (Eq. (94)) and assign to $\{\tilde{p}^{(1)}\}_{n+1}^p$ (the last-solution extrapolation predictor (Eq. (99)));
3. Form the right-hand term of Eq. (89), compute $\{u\}_{n+1}$ and $\{p\}_{n+1}$ in ABAQUS by using an implicit method;
4. Calculate the modal hydrodynamic pressure $\{\tilde{p}\}_{n+1}$ by using Eq. (91) and form the right-hand term of Eq. (93).
5. Compute $\{z_{A,j}\}_{n+1}$ in home code for each mode by using the implicit method;
6. Increment n to $n + 1$ and go to Step 2.

From the point of view of wave propagation, this high-order doubly asymptotic open boundary is spatially global as all the degrees of freedom are coupled via the eigenvectors $[\Phi]$ as shown in Eq. (38). In its numerical implementation shown in Eq. (89), the Sommerfeld boundary term expressed as the damping matrix

Table 1
Computer time for doubly asymptotic open boundaries of various orders.

Order (MH = ML)	5	10	15	20
CPU time (sec.)	18.99	27.80	36.17	44.75

Table 2
Computer time for doubly asymptotic open boundaries with various time durations of analysis.

Time durations ($\bar{t} = tc/h$)	20	40	60	80
CPU time (sec.)	6.92	13.78	20.75	27.80

is spatially local. The term $[\Phi]^{-T} \langle \lambda_j \rangle \{\tilde{p}^{(1)}\}/h$ is obtained by solving a system of decoupled equations (Eq. (93)) whose number of equations is equal to the number of degrees of freedom on the truncated boundary. Therefore, from the point of view of computational cost, this open boundary condition is spatially local.

8. Numerical examples

Two numerical examples are analyzed to evaluate the accuracy and efficiency of the present doubly asymptotic open boundary condition. The first example is a rigid dam with a vertical upstream face and a semi-infinite reservoir of constant depth. The doubly asymptotic open boundary is applied directly on the upstream face of the dam. The computational efficiency of the present technique is evaluated by measuring the computer time. The accuracy of the results is assessed by comparing with the analytical solution obtained by Chopra [2]. The second example is a flexible dam with an irregular near filed of the reservoir. The open boundary is employed to represent the regular far field of the reservoir. The results are compared with extended mesh solutions.

The time integration of Eqs. (89) and (93) are both performed by using the implicit Newmark method with $\gamma = 0.5$ and $\beta = 0.25$ (i.e. trapezoidal integration).

8.1. Rigid dam

A rigid dam with a vertical upstream face is shown in Fig. 4. The constant depth of the reservoir extending to infinity is $h = 180$ m. The pressure wave velocity is $c = 1438.7$ m/s and the density is $\rho = 1000$ kg/m³. The high-order doubly asymptotic open boundary is directly applied on the interface between rigid dam and reservoir. Twelve 3-node quadratic line elements are used to discretize the interface and the nodal interval is 7.5 m. The coupling with ABAQUS is not required. Eq. (84) replaces Eq. (89) in the sequential staggered implicit-implicit partitioned procedure with the last-solution extrapolation predictor (Eq. (99)).

The horizontal acceleration of the rigid dam is prescribed as a Ricker wavelet described by

$$a(t) = A_R \left(1 - 2 \left(\frac{t - t_s}{t_0} \right)^2 \right) \exp \left(- \left(\frac{t - t_s}{t_0} \right)^2 \right), \tag{100}$$

where t_s is the time when the wavelet reaches its maximum, $2/t_0$ is the dominant angular frequency of the wavelet and A_R is the amplitude. The Fourier transform of the wavelet is given as

$$A(\omega) = 0.5 \sqrt{\pi} A_R t_0 (\omega t_0)^2 e^{-0.25(\omega t_0)^2}. \tag{101}$$

The first cut-off frequency of the reservoir is $\omega_1 = \pi c/2h$ which corresponds to a dimensionless frequency $a_0 = \omega h/c = \pi/2$. The parameters of the Ricker wavelet are chosen as $\bar{t}_s = t_s/h = 5$, $\bar{t}_0 = t_0 c/h = 4/\pi$ and $A_R = 1$. Its dominant frequency is equal to

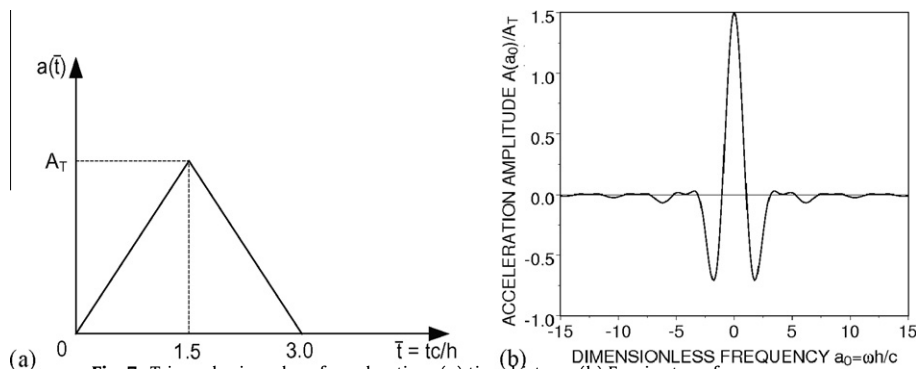


Fig. 7. Triangular impulse of acceleration: (a) time history; (b) Fourier transform.

the first cut-off frequency of the reservoir. The time history and Fourier transform of the Ricker wavelet are shown in Fig. 5(a) and (b), respectively. The time step $\Delta t = 0.001h/c$ is chosen.

The singly asymptotic boundary condition constructed by including only the high-frequency expansion is investigated. It is demonstrated in Ref. [19] that this boundary condition is closely related to several high-order transmitting boundaries. When the excitation frequency is lower than the cut-off frequency of a mode, “fictitious reflections” are observed in a long-time analysis of the modal response. For the case of the rigid dam, the hydrodynamic pressure responses at the dam heel are computed with the singly asymptotic boundary condition of orders $M_H = 11$, $M_H = 21$ and $M_H = 99$. The results are plotted in Fig. 6(a). The analytical solution [2] is shown for comparison. The responses are accurate at early time, but “fictitious reflections” occur at late time (for clarity, the results for $M_H = 11$ and $M_H = 21$ are only plotted up to the arrival of “fictitious reflections”). Although the arrival time of the “fictitious reflections” increases with the order of boundary condition, the rate of increase is slow. It is only after the order is increased to $M_H = 99$ that a reasonably accurate result is obtained for a duration of $\bar{t} = tc/h = 80$. Therefore, singly asymptotic boundaries are not suitable for long-time computation of dam–reservoir interaction.

The doubly asymptotic boundary condition leads to a significant improvement in accuracy at the same computational cost. The sin-

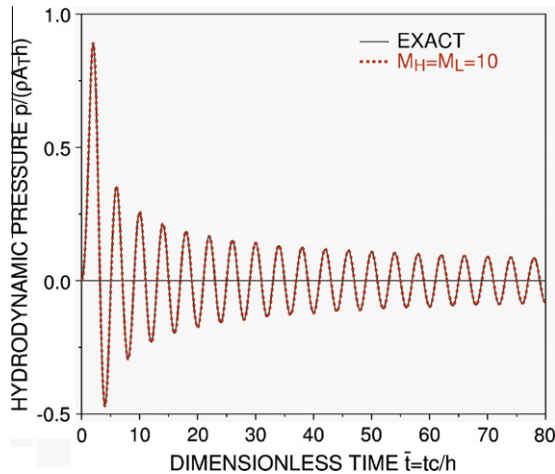


Fig. 8. Hydrodynamic pressure at heel of dam due to triangular impulse load.

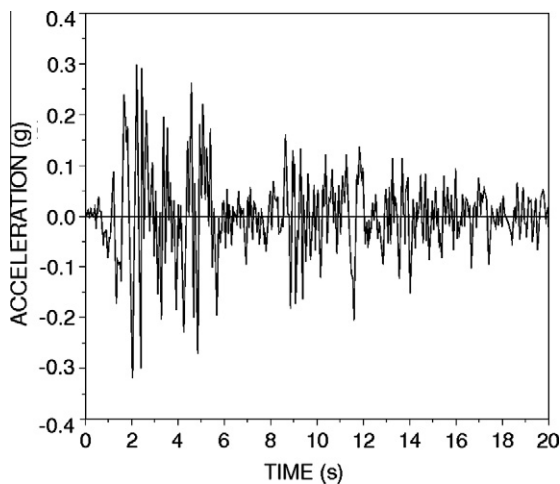


Fig. 9. Time history of El Centro earthquake.

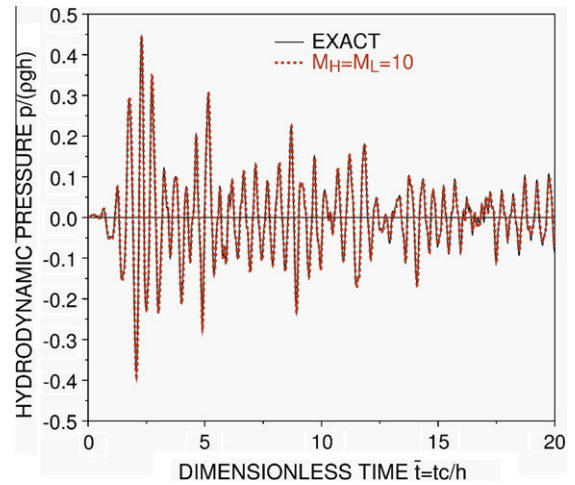


Fig. 10. Hydrodynamic pressure at heel of the dam due to earthquake.

gly asymptotic boundary conditions of orders $M_H = 11$ and $M_H = 21$ have 12 terms and 22 terms, respectively, in the continued fraction solution of dynamic stiffness. The orders of the doubly asymptotic boundary conditions having the same number of terms are $M_H = M_L = 5$ and $M_H = M_L = 10$, respectively. The results obtained with them are plotted in Fig. 6(b). It is observed that “fictitious reflections” do not occur as expected from the investigation on a single mode.[19]. By comparing Fig. 6(b) with (a), it can be found that the doubly asymptotic boundary is much more accurate than the singly asymptotic boundary with the same number of terms. The $M_H = M_L = 10$ doubly asymptotic boundary condition is even more accurate than the $M_H = 99$ singly asymptotic boundary condition.

The computer time is recorded on a laptop with a 2.53 GHz dual-core CPU. For an analysis of 80000 time steps, the computer time of the present high-order doubly asymptotic boundary are listed in Table 1 for open boundaries of orders $M_H = M_L = 5, =10, =15$ and $=20$. It is observed that the computer time increases linearly with the order of the open boundary. The increase in computer time with the number of time steps is also investigated. By using the order $M_H = M_L = 10$ boundary condition, the analyses are performed for durations of dimensionless time $\bar{t} = tc/h = 20, 40, 60$ and 80 . The computer time is shown in Table 2. As expected for this temporally local open boundary, the computer time increases linearly with the number of time steps.

A triangular impulse of acceleration that has different frequency characteristics from the Ricker wavelet is addressed. The triangular impulse $a(t)$ with a duration $3h/c$ and a peak value A_T is shown in Fig. 7(a). Its Fourier transform $A(\omega)$ is illustrated in Fig. 7(b). The time step is chosen as $\Delta t = 0.001h/c$. The hydrodynamic pressure at the heel of dam is plotted in Fig. 8. The result obtained with the order $M_H = M_L = 10$ doubly asymptotic boundary is in excellent agreement with the analytical solution.

To investigate the performance of the presented doubly asymptotic open boundary under earthquake load, the El Centro earthquake ground motions in the direction of North–South is applied (see Fig. 9). The size of time step is selected as $\Delta t = 0.0001$ s. The order of the doubly asymptotic boundary is $M_H = M_L = 10$. The hydrodynamic pressure response at the heel of dam is shown in Fig. 10. Again, no fictitious reflections occur. Excellent agreement with the analytical solution is achieved.

8.2. Flexible dam

A typical flexible gravity dam–reservoir system with an irregular near field is shown in Fig. 11(a). The dam body has a modulus of

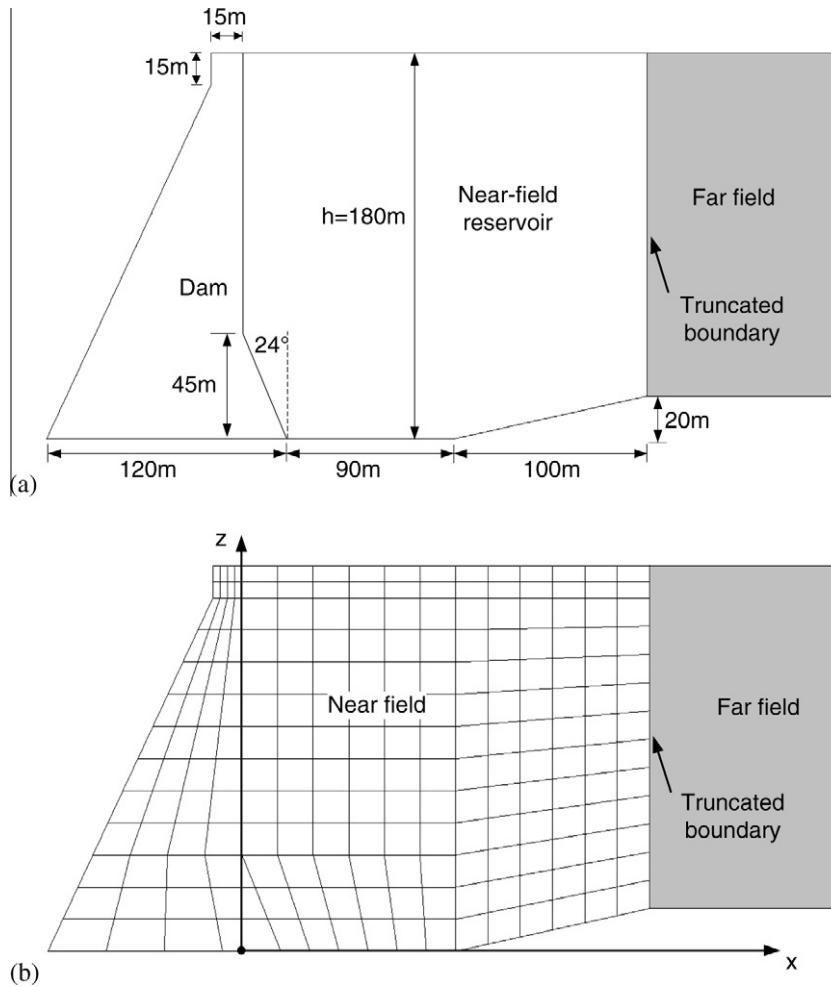


Fig. 11. A gravity dam–reservoir system with irregular near field: (a) geometry; (b) mesh.

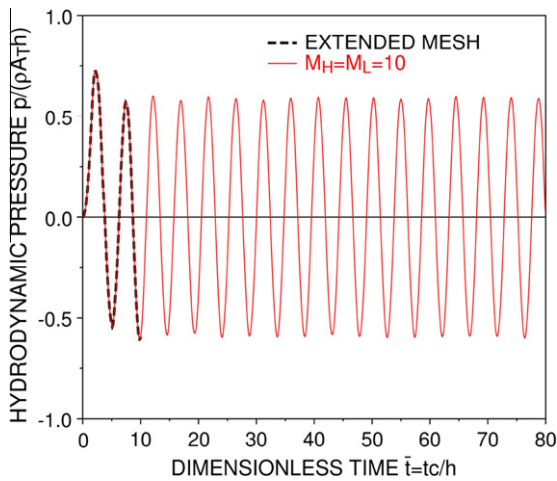


Fig. 12. Hydrodynamic pressure at heel of dam under triangular-impulse acceleration.

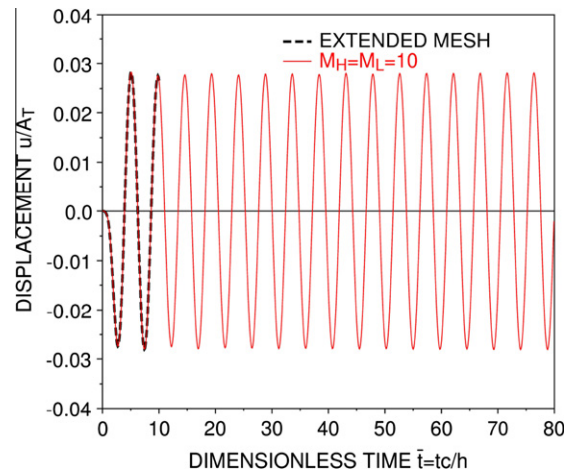


Fig. 13. Horizontal displacement at crest of dam under triangular-impulse acceleration.

elasticity $E = 35 \text{ GPa}$, Poisson's ratio $\nu = 0.2$ and mass density $\rho = 2400 \text{ kg/m}^3$. The physical property of water is the same as that in the example of the rigid dam.

The finite element mesh is shown in Fig. 11(b). The system is divided into three parts: the dam body, the near-field reservoir and the far-field reservoir with constant depth. The dam body is dis-

cretized with 52 eight-node solid elements, and the near-field reservoir with 156 eight-node acoustic fluid elements. The solid elements and acoustic fluid elements are coupled on the upstream dam face by 13 three-node interface elements. The far-field reservoir is modeled by 13 three-node quadratic line elements. The elements share the same nodes and are compatible on the truncated

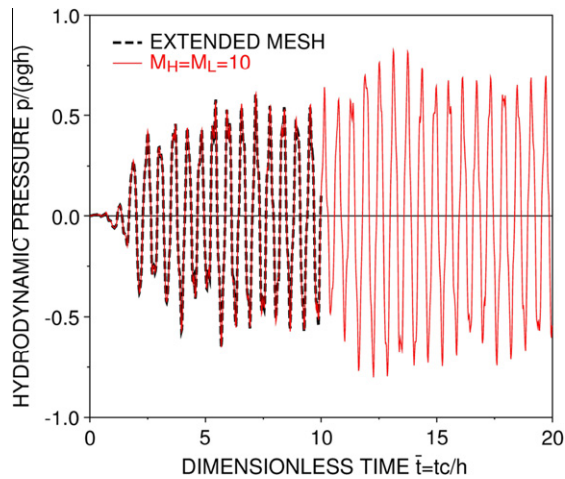


Fig. 14. Hydrodynamic pressure at heel of dam under El Centro ground motion.

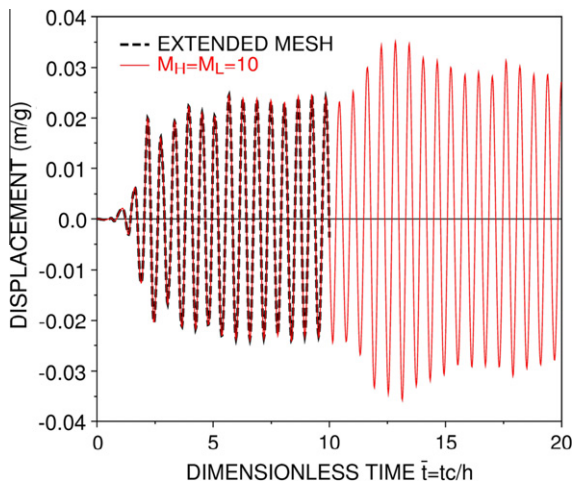


Fig. 15. Horizontal displacement at crest of dam under El Centro ground motion.

boundary with those of the near-field acoustic fluid elements. The total number of nodes in the whole model is 653.

The triangular impulse (Fig. 7) is imposed as the horizontal acceleration at the base of the dam. The time step is $\Delta t = 0.01h/c$. During one time step, the pressure waves travel about one quarter of the distance between two adjacent nodes. 8000 time steps are computed. The responses of the hydrodynamic pressure at the heel of dam and the horizontal displacement at the crest of dam are shown in Figs. 12 and 13, respectively. To verify the results, an extended mesh covering a far-field reservoir region of 7200 m is analysed. This region is discretized with 5733 eight-node elements of uniform size (not shown). The total number of nodes is 18067. The size of extended mesh is sufficiently large to avoid the pollution of the dam response by the waves reflected on the truncated boundary for a time duration of $t = 80h/c \approx 10$ s. Excellent agreement between the present solutions and the extended mesh solutions is observed.

The response of the dam–reservoir system subjected to the El Centro earthquake ground motion (Fig. 9) is analyzed. The time step is chosen as 0.002 s during which the pressure wave travels about one third of the distance between two adjacent nodes. The responses of the first 20 s are plotted in Fig. 14 for the hydrodynamic pressure at the heel of dam and in Fig. 15 for the horizontal displacement at the crest of dam. The results agree very well with

the extended mesh solutions during the first 10 s (before the waves reflected on the truncated boundary arrive at the dam).

9. Conclusions

A high-order doubly asymptotic open boundary condition is developed for evaluating the hydrodynamic pressure in a semi-infinite reservoir of constant depth. It is established on a vertical truncated boundary by using the scaled boundary finite element method. The same isoparametric finite elements are used in modeling the near field and the far field of a semi-infinite reservoir. The open boundary condition is split into the Sommerfeld radiation boundary and an external nodal load. Making use of the restart function in the general-purpose finite element package ABAQUS, the response of the gravity dam–reservoir system is solved by a sequential staggered implicit-implicit partitioned procedure. From the point of view of computational cost, this boundary condition is local in both space and time. Numerical examples demonstrate the excellent performance of this present technique for not only early-time but also long-time computations. The open boundary condition is stable and converges rapidly as the order increases.

References

- [1] Westergaard HM. Water pressure on dams during earthquakes. *Trans Am Soc Civil Eng* 1933;98:418–33.
- [2] Chopra AK. Hydrodynamic pressures on dams during earthquakes. *J Eng Mech Div* 1967;93(EM6):205–23.
- [3] Chwang AT. Hydrodynamic pressures on sloping dams during earthquakes 2. Exact theory. *J Fluid Mech* 1978;87(Jul):343–8.
- [4] Chwang AT, Housner GW. Hydrodynamic pressures on sloping dams during earthquakes. 1. Momentum method. *J Fluid Mech* 1978;87(July):335–41.
- [5] Chopra AK. Earthquake response of concrete gravity dams. *J Eng Mech Div-Asce* 1970;96(4):443–54.
- [6] Chakrabarti P, Chopra AK. Earthquake analysis of gravity dams including hydrodynamic interaction. *Earthquake Eng Struct Dyn* 1973;2(2):143–60.
- [7] Saini S S, Bettess P, Zienkiewicz OC. Coupled hydrodynamic response of concrete gravity dams using finite and infinite elements. *Earthquake Eng Struct Dyn* 1978;6(4):363–74.
- [8] Chopra AK, Chakrabarti P. Earthquake analysis of concrete gravity dams including dam–water–foundation rock interaction. *Earthquake Eng Struct Dyn* 1981;9(4):363–83.
- [9] Hall JF, Chopra AK. Two-dimensional dynamic analysis of concrete gravity and embankment dams including hydrodynamic effects. *Earthquake Eng Struct Dyn* 1982;10(2):305–32.
- [10] Zienkiewicz OC, Bettess P. Fluid–structure dynamic interaction and wave forces: an introduction to numerical treatment. *Int J Numer Methods Eng* 1978;13(1):1–16.
- [11] Tsai CS, Lee GC, Ketter RL. A semi-analytical method for time-domain analyses of dam–reservoir interactions. *Int J Numer Methods Eng* 1990;29(5):913–33.
- [12] Tsai CS, Lee GC. Time-domain analyses of dam–reservoir system. II: substructure method. *J Eng Mech* 1991;117(9):2007–26.
- [13] Yang R, Tsai CS, Lee GC. Explicit time-domain transmitting boundary for dam–reservoir interaction analysis. *Int J Numer Methods Eng* 1993;36(11):1789–804.
- [14] Touhei T, Ohmachi T. A FE-BE method for dynamic analysis of dam foundation reservoir systems in the time domain. *Earthquake Eng Struct Dyn* 1993;22(3):195–209.
- [15] Camara RJ. A method for coupled arch dam–foundation–reservoir seismic behaviour analysis. *Earthquake Eng Struct Dyn* 2000;29(4):441–60.
- [16] Czygan O, von Estorff O. Fluid–structure interaction by coupling BEM and nonlinear FEM. *Eng Anal Bound Elem* 2002;26(9):773–9.
- [17] Tsynkov SV. Numerical solution of problems on unbounded domains: a review. *Appl Numer Math* 1998;27(4):465–532.
- [18] Givoli D. High-order local non-reflecting boundary conditions: a review. *Wave Motion* 2004;39(4):319–26.
- [19] Prempramote S, Song C, Tin-Loi F, Lin G. High-order doubly asymptotic open boundaries for scalar wave equation. *Int J Numer Methods Eng* 2009;79(3):340–74.
- [20] Geers T. Singly and doubly asymptotic computational boundaries. In: TL G, editor. *Proceedings of the IUTAM symposium on computational methods for unbounded domains*. Dordrecht: Kluwer Academic Publishers; 1998. p. 135–41.
- [21] Geers TL. Doubly asymptotic approximations for transient motions of submerged structures. *J Acoust Soc Am* 1978;64(5):1500–8.
- [22] Underwood P, Geers TL. Doubly asymptotic, boundary-element analysis of dynamic soil–structure interaction. *Int J Solids Struct* 1981;17(7):687–97.

- [23] Geers T, Zhang P. Doubly asymptotic approximations for submerged structures with internal fluid volumes. *J Appl Mech* 1994;61:893–906.
- [24] Geers T, Lewis B. Doubly asymptotic approximations for transient elastodynamics. *Int J Solids Struct* 1997;34:1293–305.
- [25] Geers T, Tothaker B. Third-order doubly asymptotic approximations for computational acoustics. *J Comput Acoust* 2000;8:101–20.
- [26] Ruge P, Trinks C, Witte S. Time-domain analysis of unbounded media using mixed-variable formulations. *Earthquake Eng Struct Dyn* 2001;30(6):899–925.
- [27] Alpert B, Greengard L, Hagstrom T. Nonreflecting boundary conditions for the time-dependent wave equation. *J Comput Phys* 2002;180(1):270–96.
- [28] Birk C, Ruge P. Representation of radiation damping in a dam-reservoir interaction analysis based on a rational stiffness approximation. *Comput Struct* 2007;85(11–14):1152–63.
- [29] Berenger JP. A perfectly matched layer for the absorption of electromagnetic waves. *J Comput Phys* 1994;114(2):185–200.
- [30] Basu U, Chopra AK. Perfectly matched layers for transient elastodynamics of unbounded domains. *Int J Numer Methods Eng* 2004;59(8):1039–74.
- [31] Bazyar MH, Song CM. A continued-fraction-based high-order transmitting boundary for wave propagation in unbounded domains of arbitrary geometry. *Int J Numer Methods Eng* 2008;74(2):209–37.
- [32] Lysmer J, Waas G. Shear waves in plane infinite structures. *J Eng Mech* 1972;98(1):85–105.
- [33] Song C, Wolf JP. The scaled boundary finite-element method – alias consistent infinitesimal finite-element cell method – for elastodynamics. *Comput Methods Appl Mech Eng* 1997;147(3–4):329–55.
- [34] Wolf JP, Song CM. The scaled boundary finite-element method – a primer: derivations. *Comput Struct* 2000;78(1–3):191–210.
- [35] Park KC. Partitioned transient analysis procedures for coupled-field problems: stability analysis. *J Appl Mech* 1980;47(2):370–6.
- [36] Park KC, Felippa CA. Partitioned transient analysis procedures for coupled-field problems: accuracy analysis. *J Appl Mech* 1980;47(4):919–26.